Journal of Power Sources 195 (2010) 1292–1301

Contents lists available at ScienceDirect

Journal of Power Sources

journal homepage: www.elsevier.com/locate/jpowsour

Minimization of the cation mixing in $Li_{1+x}(NMC)_{1-x}O_2$ as cathode material

Xiaoyu Zhang[a,c], W.J. Jiang[b], A. Mauger[c], Qilu[a,*], F. Gendron[d], C.M. Julien[d]

[a] Department of Applied Chemistry, College of Chemistry and Molecular Engineering, Peking University, Beijing 100871, PR China
[b] CITIC Guoan Mengguli New Energy Technology Co. Ltd., Beijing 102200, PR China
[c] Institut de Minéralogie et de Physique des Milieux Condensée, Université Pierre et Marie Curie, 140 rue de Lourmel, 75015 Paris, France
[d] Institut des Nanosciences de Paris, Université Pierre et Marie Curie, 140 rue de Lourmel, 75015 Paris, France

ARTICLE INFO

Article history:
Received 8 July 2009
Received in revised form 7 September 2009
Accepted 10 September 2009
Available online 20 September 2009

Keywords:
$LiNi_{1/3}Mn_{1/3}Co_{1/3}O_2$
Co-precipitation method
Rietveld refinement
Magnetic properties
Lithium-ion batteries

ABSTRACT

$Li_{1+x}(Ni_{1/3}Mn_{1/3}Co_{1/3})_{1-x}O_2$ layered materials were synthesized by the co-precipitation method with different Li/*M* molar ratios (*M* = Ni + Mn + Co). Elemental titration evaluated by inductively coupled plasma spectrometry (ICP), structural properties studied by X-ray diffraction (XRD), Rietveld analysis of XRD data, scanning electron microscopy (SEM) and magnetic measurements carried out by superconducting quantum interference devices (SQUID) showed the well-defined α-$NaFeO_2$ structure with cationic distribution close to the nominal formula. The Li/Ni cation mixing on the 3*b* Wyckoff site of the interlayer space was consistent with the structural model $[Li_{1-y}Ni_y]_{3b}[Li_{x+y}Ni_{(1-x)/3-y}Mn_{(1-x)/3}Co_{(1-x)/3}]_{3a}O_2$ ($x = 0.02, 0.04$) and was very small. Both Rietveld refinements and magnetic measurements revealed a concentration of Ni^{2+}-3*b* ions lower than 2%; moreover, for the optimized sample synthesized at Li/*M* = 1.10, only 1.43% of nickel ions were located into the Li sublattice. Electrochemical properties were investigated by galvanostatic charge–discharge cycling. Data obtained with $Li_{1+x}(Ni_{1/3}Mn_{1/3}Co_{1/3})_{1-x}O_2$ reflected the high degree of sample optimization. An initial discharge capacity of 150 mAh g^{-1} was delivered at 1 C-rate in the cut-off voltage of 3.0–4.3 V. More than 95% of its initial capacity was retained after 30 cycles at 1 C-rate. Finally, it is demonstrated that a cation mixing below 2% is considered as the threshold for which the electrochemical performance does not change for $Li_{1+x}(Ni_{1/3}Mn_{1/3}Co_{1/3})_{1-x}O_2$.

1. Introduction

Although $LiCoO_2$ has formed the basis of cathode electrode in commercial lithium-ion batteries (LIBs), its relatively high cost, toxic properties, practically reachable capacity of only 50% of the theoretical capacity and safety problem inhibit its further use in price-sensitive and large-scale applications, such as electric vehicles (EVs) and hybrid electric vehicles (HEVs) [1,2]. So researchers worldwide are searching for high-capacity, safe, and inexpensive replacement for $LiCoO_2$. Nowadays, a layered transition-metal oxide $LiNi_{1/3}Mn_{1/3}Co_{1/3}O_2$ (named LNMCO hereafter) with hexagonal structure, first introduced by Ohzuku's group in 2001 as a candidate of cathode materials [3,4], has attracted significant interest, because the combination of nickel, manganese, and cobalt can provide many advantages compared with $LiCoO_2$, such as lower cost, less toxicity, milder thermal stability at charged state, better stability during cycling even at elevated temperature, and higher reversible capacity [5–7]. It has been demonstrated that the charge compensation is achieved by stabilization of Ni^{2+}, Mn^{4+} and Co^{3+} ions [8,9]. The electrochemical reaction of lithium extraction/insertion takes place by oxidation/reduction of Ni^{2+}/Ni^{4+} and Co^{3+}/Co^{4+} ions depending on different cut-off voltages, while Mn^{4+} remains inactive but maintains the structural stability [10]. Therefore, LNMCO might be a promising candidate of cathode material for the next generation of high-power and high-energy LIBs [11].

However, the cation mixing between lithium and nickel ions on the crystallographic 3*b* site of the LNMCO lattice, which is known to deteriorate the electrochemical performance of layered oxides, still remains a severe problem [12]. Since the ionic radius of Li^+ (0.76 Å) is close to that of Ni^{2+} (0.69 Å), a partial occupation of Ni^{2+} lattice sites by Li^+ (by interchange between a Li^+ ion and a nearest neighbor Ni^{2+} ion to insure local charge neutrality and minimize Coulomb energy) generates a cation mixing in the structure, which blocks the pathway of lithium diffusion [13,14].

The aim of this work is the optimization of electrode materials for Li-ion batteries by adjusting one parameter of the synthesis, namely the lithium/transition-metal ratio, so as to minimize the cation mixing. Two independent experimental procedures are used to estimate the cation mixing: (i) magnetic measurements, which are powerful tools to check the quality of samples and structural properties at nanoscopic scale [15], especially in the case of transition-metal oxides; (ii) structural refinements of XRD patterns made by Rietveld method, which accurately determine the transition-metal occupancy between the slab of this layered mate-

* Corresponding author. Tel.: +86 10 62751000; fax: +86 10 62755290.
E-mail address: qilu@pku.edu.cn (Qilu).

0378-7753/$ – see front matter © 2009 Elsevier B.V. All rights reserved.
doi:10.1016/j.jpowsour.2009.09.029

rial [16]. It is well-established that the presence of Ni^{2+} ions onto the 3*b* site of the lithium sublattice (noted $Ni^{2+}(3b)$ hereafter) can generate a ferromagnetic interaction with the Mn^{4+} ions nearest neighbors on 3*a* sites, and this $Ni^{2+}(3b)$–$Mn^{4+}(3a)$ ferromagnetic interaction results in the formation of a ferromagnetic cluster centred on the $Ni^{2+}(3b)$ defect [17,18]. The magnetic moment of these ferromagnetic clusters can be accessed by the magnetic measurements, from which the concentration of the $Ni^{2+}(3b)$ defects can be deduced and compared with the concentration deduced from Rietveld refinement [19]. This paper is then focussed on the investigation of these important structural features and their correlation with the magnetic of $Li_{1+x}(Ni_{1/3}Mn_{1/3}Co_{1/3})_{1-x}O_2$ samples as a function of the synthetic conditions. The electrochemical behaviours of the $Li_{1+x}(Ni_{1/3}Mn_{1/3}Co_{1/3})_{1-x}O_2$ electrode materials synthesized by co-precipitation method are investigated in Li cells and data are discussed in detail.

2. Experimental

2.1. Sample preparation

The synthesis of $Li_{1+x}(Ni_{1/3}Mn_{1/3}Co_{1/3})_{1-x}O_2$ powders were performed by a hydroxide route using transition-metal hydroxide and lithium carbonate as starting materials. First, the synthesis of transition-metal hydroxide of composition $(Ni_{1/3}Mn_{1/3}Co_{1/3})(OH)_2$ was realized using $NiSO_4{\cdot}6H_2O$, $MnSO_4{\cdot}6H_2O$, $CoSO_4{\cdot}6H_2O$, NaOH and NH_4OH (analysis grade) as raw materials dissolved in distilled water. An aqueous solution prepared with a concentration of 2 mol L^{-1} was pumped into a continuously stirred tank reactor. At the same time, NaOH and NH_4OH solution was also fed into the reactor, in which the pH was controlled with care to its optimized value, namely 11 [14].

After vigorous stirring at 40–60 °C for 12 h, the homogenously precipitated hydroxide powder $(Ni_{1/3}Mn_{1/3}Co_{1/3})(OH)_2$ was filtered off and dried at 120 °C for 12 h. The second step consisted in mixing appropriate amount of lithium carbonate Li_2CO_3 and $(Ni_{1/3}Mn_{1/3}Co_{1/3})(OH)_2$ with various molar ratio η of Li to M = Ni + Mn + Co larger than unity. This excess of alkali in the preparation process as well as the presence of oxygen during precipitation reaction has been recognized to facilitate the formation of compounds containing manganese and oxygen elements [20]. First, the excess in Li is intended to compensate the loss of lithium through evaporation during the calcination. In addition, Myung et al. [21] have shown that an excess of lithium counteracted the Li–Ni cation mixing for the system $Li_{1+x}(Ni_{0.5}Mn_{0.5})_{1-x}O_2$, and it is also true for the compound of the present study [22]. Indeed, studies have shown that a lithium excess promotes the electrochemical performance for the LNMCO material too [23,24], which can be attributable to this reduction in the cation mixing, although it has not been evaluated in these prior works. After suitable grounding and stirring, the mixture was heated at 500 °C for 5 h. The final $Li_{1+x}(Ni_{1/3}Mn_{1/3}Co_{1/3})_{1-x}O_2$ products were fired at 950 °C for 10 h in air. The samples described here were obtained with nominal values η = Li/M = 1.05 (sample A) and 1.10 (sample B), which led to optimized results.

2.2. Characterization

The elemental analysis of $Li_{1+x}(Ni_{1/3}Mn_{1/3}Co_{1/3})_{1-x}O_2$ was carried out by an inductively coupled plasma spectrometer (ICP, Optima 4300DV, PE Ltd.). The structure was characterized by X-ray diffraction (XRD) on a Philips X'Pert PRO MRD (PW3050) diffractometer equipped with a Cu anticathode (Cu Kα radiation λ = 1.54056 Å) at room temperature. XRD patterns were collected under Bragg–Brentano geometry at 2θ with step 0.02° in the range 10–80°. Profile refinement of the XRD patterns was made using the GSAS/EXPGUI version of the Rietveld package [25]. The surface morphology and particle size distribution were examined by scanning electron microscopy (SEM, JEOL JSM-5600LV microscope).

Table 1
Results of the ICP analysis for two samples of $Li_{1+x}(Ni_{1/3}Mn_{1/3}Co_{1/3})_{1-x}O_2$ (x = 0.02, 0.04).

Sample	Nominal ratio Li/M	Molar ratio of the final product (±1%)			
		Li	Ni	Mn	Co
A	1.05	1.02	0.32	0.33	0.33
B	1.10	1.04	0.32	0.32	0.32

The magnetic measurements (susceptibility and magnetization) were performed with fully automated SQUID magnetometer (Quantum Design MPMS XL) in the temperature range 4–300 K. Powders were placed into small plastic vial, placed in a holder and finally inserted into the helium cryostat of the SQUID apparatus. The temperature dependence of the susceptibility data was recorded during heating of the sample using two modes: zero-field cooling (ZFC) and field cooling (FC), to determine the magnetic behaviour. The procedure is based on performing two consecutive magnetization measurements: in ZFC the sample is first cooled down in the absence of magnetic field, then a magnetic field H = 10 kOe is applied, and the ZFC magnetic susceptibility $M(T)/H$ where M is the magnetization is measured upon heating. In the FC experiments, the same magnetic field is applied first at room temperature; the FC susceptibility is measured upon cooling. No difference, i.e. no magnetic irreversibility effect has been detected between ZFC and FC measurements in any of the samples. Magnetic curves $M(H)$ have been measured in an applied magnetic field in a range 0–30 kOe.

2.3. Electrochemical measurements

Charge–discharge tests were performed on coin type cell (CR2032). Composite positive electrode was prepared by thoroughly mixing the active material (90 wt%) with carbon black (2 wt%), acetylene black (2 wt%), polyvinylidene fluoride (6 wt%) in N-methyl-pyrrolidinone and spread onto aluminium foils then dried for 24 h at 120 °C in vacuum. Cells were then assembled in an argon-filled glove box (Braun, Germany) using foils of Li metal as counter electrode and Celgard 2400 as separator. The electrolyte was 1.0 mol L^{-1} $LiPF_6$ in a mixture of ethylene carbonate (EC) and diethyl carbonate (DEC) (1:1, v/v). The cells were galvanostatically cycled between 3.0 and 4.3 V vs. Li^0/Li^+ on a Land CT2001A battery tester (China, Wuhan Jinnuo Electronics Co. Ltd.) at room temperature.

3. Results and discussion

3.1. Structure and morphology

Elemental titration of samples A and B synthesized with nominal Li/M ratio η = 1.05 and 1.10, respectively, have been evaluated by inductively coupled plasma (ICP) spectroscopy. The results, reported in Table 1, show that the technological composition for each metal in $Li_{1+x}(Ni_{1/3}Mn_{1/3}Co_{1/3})_{1-x}O_2$ is close to the stoichiometry and we obtained lithium-rich samples $Li_{1+x}(Ni_{1/3}Mn_{1/3}Co_{1/3})_{1-x}O_2$ with x = 0.02 and 0.04 for samples A and B, respectively. Note that the Li/M ratios of the sample are $(1+x)/(1-x)$ = 1.04 and 1.08 for the samples A and B, respectively, close to the nominal ratio η. This gives evidence that the amount of Li that has evaporated during the synthesis is very small (1–2% only), and comparable to the case when the samples are prepared by the Pechini method [26]. As a consequence, the excess of lithium introduced in the preparation process cannot be adjusted to com-

Table 2
Lattice parameters a, c, c/a of two samples of $Li_{1+x}(Ni_{1/3}Mn_{1/3}Co_{1/3})_{1-x}O_2$ ($x = 0.02, 0.04$), synthesized by co-precipitation method. V is the volume of the unit cell, L is the lattice coherence length in the plane perpendicular to the c-axis. The last column is the ratio of the intensities of the XRD lines labelled by their Miller indexes and $r_I = (I_{006} + I_{102})/I_{101}$.

Sample	a (Å)	c (Å)	c/a	V (Å^3)	L (nm)	r_I	I_{003}/I_{104}
A	2.8650(1)	14.252(2)	4.9745(9)	101.31(2)	59.4(4)	0.417	1.407
B	2.8603(2)	14.241(2)	4.9788(10)	100.90(3)	55.9(4)	0.393	1.482

pensate exactly the evaporation of lithium during the sintering of the sample, so that at the end, the final product still contains a small excess of Li, in relative concentration x, which substitutes to a transition-metal ion to form $Li_{1+x}(Ni_{1/3}Mn_{1/3}Co_{1/3})_{1-x}O_2$. The reason is that the sintering temperature T_s during the synthesis is 950 °C only. Important evaporation of Li takes palace for T_s >1000 °C in this material [26], and in similar oxides as well [27]. This result might suggest that the excess in lithium in the preparation process should be reduced to get a final product closer to stoichiometry. However, we shall see hereunder that the major advantage of this excess in lithium is the reduction of cation mixing.

Fig. 1 shows powder XRD patterns of samples A and B. All the diffraction lines are well indexed in the rhombohedral system with $R\bar{3}m$ space group. Both XRD diagrams display a single-phase α-$NaFeO_2$-type structure without any impurity phase. As seen in Fig. 1, both the (0 0 6)/(1 0 2) and (1 0 8)/(1 1 0) doublets are well separated, which indicates a good hexagonal ordering of layered LNMCO materials [28,29]. According to Dahn et al. [30,31], the r_I-factor defined by $(I_{006}+I_{102})/I_{101}$ is an indicator of the hexagonal ordering; the lower the r_I, the better the hexagonal ordering. The values of r_I of the two samples are reported in Table 2. Sample B has a lower r_I, which indicates better hexagonal ordering of its lattice than that of the A-sample. In addition, the integrated intensity ratio of (0 0 3) to (1 0 4) peaks, I_{003}/I_{104}, also reported in Table 2, is considered as a sensitive parameter to determine the cationic distribution in the in the α-$NaFeO_2$-type lattice [32]. The smaller I_{003}/I_{104} is, the higher structural deviation is from hexagonal towards cubic symmetry. A value less than 1.2 means that undesirable cation mixing would appear. For our $Li_{1+x}(Ni_{1/3}Mn_{1/3}Co_{1/3})_{1-x}O_2$ powders synthesized by the hydroxide route, we find I_{003}/I_{104} = 1.407 and 1.482 for samples A and B, respectively, which suggests that the cation mixing is very weak in both samples. However, we observe that the B-sample displays better structural integrity (lower r_I value and higher I_{003}/I_{104} value), which gives evidence that the cation mixing is smaller in the sample prepared from lithium-rich composition.

The narrow profile of the diffraction lines indicates a high crystallinity of the $Li_{1+x}(Ni_{1/3}Mn_{1/3}Co_{1/3})_{1-x}O_2$ powders and suggests

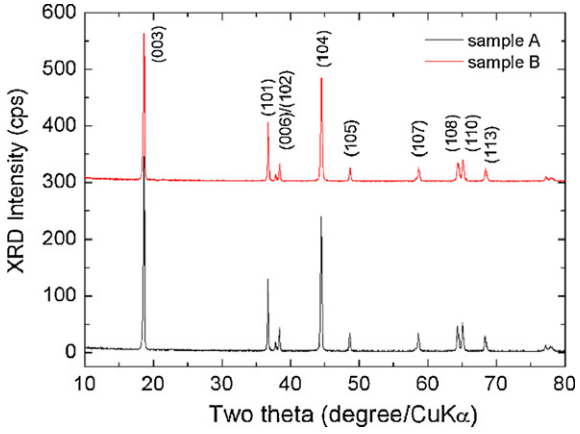

Fig. 1. XRD patterns of $Li_{1+x}(Ni_{1/3}Mn_{1/3}Co_{1/3})_{1-x}O_2$ synthesized with different η = Li/M ratios: η = 1.05 and 1.10 for samples A and B, respectively. Powder were fired at 950 °C for 10 h in air.

a homogeneous distribution of cations within the structure. The mean lattice coherence length L was calculated from XRD patterns, using Scherrer's formula

$$L = \frac{K \cdot \lambda}{\beta \cdot \cos\theta}, \quad (1)$$

where β is the width of any Bragg line in radians, the constant is K = 0.9, λ is the wavelength of the X-ray, θ is the corresponding Bragg angle, and L is the value of MCDS. The Scherrer's formula has been applied to three main XRD lines, namely (0 0 3), (1 0 1) and (1 0 4). Due to the hexagonal structure that implies non-spherical crystallites, the coherence length was found different for the three lines considered with the hierarchy: $L_{003} > L_{101} > L_{104}$. The mean crystallite size L_{003} in the [0 0 1] direction is about 80 Å larger than in the perpendicular direction, which is linked to the elongated shape of the crystallites. The mean values of L are listed in Table 2. L significantly depends on the lithium–metal ratio in the synthesis. The higher the Li/M ratio, the smaller particle size is. We shall see hereunder that the increase of the Li/M ratio induces an increased rate of substitution of Ni by Li, and thus disorder in the M-slabs that is responsible for the reduction of L.

Rietveld refinements have been made as follows. We start with the constraints that at stoichiometry, lithium-ion occupy the 3b (0, 0, 0) Wyckoff sites the nickel–manganese–cobalt ions occupy the 3a (0, 0, 1/2) Wyckoff sites, while the oxygen anions occupy the 6c (0, 0, z_{oxy}) position. In addition, we assume each cationic site is fully occupied and the number of cations equals that of anions so the overall charge neutrality is maintained. Then, excess in lithium is constrained to occupy 3b (0, 0, 0) sites, in substitution to a transition-metal ion. The constraints imposed to the Rietveld refinement of the $Li_{1+x}(Ni_{1/3}Mn_{1/3}Co_{1/3})_{1-x}O_2$ compounds are then

$$\sum_i \xi_i [C_i] = 1, \quad (2)$$

$$\sum_i \xi_i Z_i = 4, \quad (3)$$

where $[C_i]$ is the concentration of the cations (the metal ions, and the lithium ions) labelled by i, irrespectively of the site they occupy, ξ_i is their occupancy rate and Z_i is their oxidation state. The first equation is the constraint that all the cationic sites are occupied, the second equation insures the charge neutrality, assuming two O^{2-} ions per chemical formula, i.e. assuming that there is no oxygen deficiency. This assumption is indeed reasonable, since we have pointed out that the co-precipitation step of the synthesis has been made in presence of oxygen.

It is well known that stoichiometric LNMCO material contains Ni^{2+}, Mn^{4+} and Co^{3+} electronic states [10]. However, due to the excess of lithium ($x > 0$), the charge neutrality according to Eq. (3) requires oxidation of a metal ion. The metal element that is oxidized is the nickel, because the oxidation of Ni^{2+} is energetically more favorable than those of Mn^{4+} and Co^{3+}. Then, the index i in Eqs. (2) and (3) runs from 1 to 4 to distinguish between Ni^{2+}, Ni^{3+}, Mn^{4+} and Co^{3+}. It is then straightforward to determine the concentration of nickel (the ξ-parameter) that has to be oxidized in the Ni^{3+} state of charge to insure the charge neutrality in the formula $Li_{1+x}(Ni_{1/3}Mn_{1/3}Co_{1/3})_{1-x}O_2$. The result is $\xi[Ni^{3+}] = 2x$ per formula.

Finally, we assumed the existence of a small amount of Ni^{2+} in the lithium sites (cation mixing), due to the smaller difference in size between the Ni^{2+}(0.69 Å) and the Li^+ ions (0.76 Å), in contrast with other cations $r(Ni^{3+}) = 0.56$ Å, $r(Mn^{4+}) = 0.53$ Å, $r(Co^{3+}) = 0.54$ Å in an octahedral environment [33]. Note, however, that a defect can be generated only if its energy of formation is small, and the material is ionic. This implies the additional constraint that Ni^{2+} and not Ni^{3+} can occupy a Li^+ site. In Kröger-Vink notation, this is the $Ni^{\bullet}_{Li}$ defect, and this charge has to be compensated by the opposite, i.e. $Li^{/}_{Ni}$, which corresponds to a Li^+ ion on a Ni^{2+}site preferentially close to it, to result in a neutral $Ni^{\bullet}_{Li} + Li^{/}_{Ni}$ pair, with one Ni^{2+} ion on a 3*b* site plus one Li^+ ion on a 3*a* site (cation mixing).

While the presence of Ni^{3+} is made possible by the formation of such pairs, thee presence of Ni^{4+} in the as-prepared material is rules out for the following reason. The presence of Ni^{4+} would require, close to it, two $Li^{/}_{Ni}$ nearest neighbors in the lattice to insure charge neutrality at the mesoscopic scale. However, this is not realistic because the change in Coulomb charge on these three (3*a*) sites plus the difference in ionic radii between Li^+ and Ni^{2+} would imply a strong local strain/distortion field to which would be associated a big energy of deformation. This energy of deformation implies that the energy of formation of this complex defect would be large, which prevents its formation in the range of temperatures used for the preparation and calcination during the synthesis process. Only the $Ni^{\bullet}_{Li} + Li^{/}_{Ni}$ defect with a low energy of formation can be generated, still in low concentration. An equivalent argument is the following: the energy of formation of a defect involving two $Li^{/}_{Ni}$ nearest neighbors being larger than the defect involving one $Li^{/}_{Ni}$ only, the interaction between two $Li^{/}_{Ni}$ is repulsive. Added to the fact that the amount of $Li^{/}_{Ni}$ is very small (few%), we can infer that the probability that two $Li^{/}_{Ni}$ are nearest neighbors vanishes.

If *y* is the concentration of $Ni^{\bullet}_{Li} + Li^{/}_{Ni}$ pair defects, the detailed chemical formula is then $[Li_{1-y}Ni_y]_{3b}[Li_{x+y}Ni_{(1-x)/3-y}Mn_{(1-x)/3}Co_{(1-x)/3}]_{3a}O_2$ for Rietveld refinements: both *x* and *y* were refined. This detailed formula already satisfies Eq. (2), and the other constraints resulting from this discussion is the following: in this detailed formula, 2*x* nickel ions on the (3*a*) sites are Ni^{3+}, all the other nickel ions in the formula are Ni^{2+} ions, the cobalt is in the trivalent state, and the manganese is in the tetravalent state. Note the detailed formula implies that we have implicitly assumed that the concentration of nickel, cobalt and manganese are equal (and constrained to be $(1-x)/3$). This is justified by the ICP measurements, and it restricts the number of refined parameters so that the refinement is reliable. The Rietveld fit of the XRD patterns for samples A and B are shown in Fig. 2a and b. The values of *x* were found in quantitative agreement with the titration analysis, and the results for the other parameters are reported in Table 2 for the lattice parameters and Table 3 for the other parameters of interest. In particular, *y* is found to be lower in sample B, a result we had anticipated from the analysis of I_{003}/I_{104}.

The *R* and χ^2 parameters of the Rietveld refinement are very good, and actually better than a prior work [26]. This is attributable to the fact that in the prior work, either *x* was set to zero, or *y* was set to zero, and indeed, both these parameters have to be considered as fitting parameters in the Rietveld refinement to reach the values in Table 3. This result also validates our approach, and suggests that the quality of the Rietveld refinement is presumably limited only by the fact that the spatial correlation between the Li^+(3*a*) and Ni^{3+}(3*a*) ions on one hand, and between Ni^{2+}(3*b*) and Li^+(3*a*) on another hand, are neglected in the refinement, while they should form pairs to insure charge neutrality at the local scale.

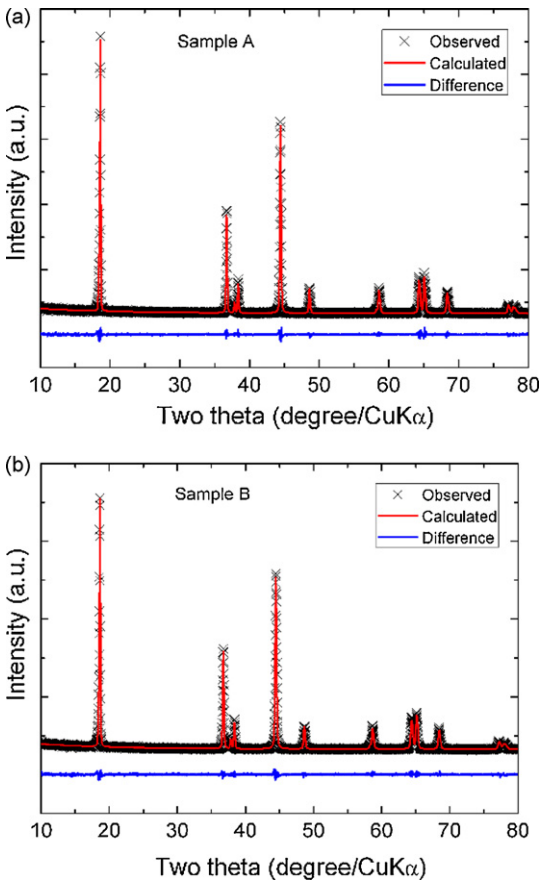

Fig. 2. Rietveld refinement patterns of $Li_{1.02}(Ni_{1/3}Mn_{1/3}Co_{1/3})_{0.98}O_2$ sample A (a) and $Li_{1.04}(Ni_{1/3}Mn_{1/3}Co_{1/3})_{0.96}O_2$ sample B (b). The cross marks show observed X-ray diffraction intensities and the solid line (in red) represents calculated intensities. The curve at the bottom (in blue) is the difference between the calculated and observed intensities on the same scale. (For interpretation of the references to color in this figure legend, the reader is referred to the web version of the article.)

The lattice parameter, *a*, is related to the average metal–metal (*M*–*M*) intra-slab distance, while *c* is related to the average *M*–*M* inter-slab distance. The substitution of Ni^{2+} ions on 3*a* sites results in two competitive effects on *a*. Since the ionic radius of Ni^{2+} is smaller than that of Li^+, the difference in ionic radii favors a decrease of *a*. On another hand, the difference of the effective ionic

Table 3
Results of the Rietveld refinements for two samples of $Li_{1+x}(Ni_{1/3}Mn_{1/3}Co_{1/3})_{1-x}O_2$ ($x = 0.02, 0.04$).

	$S(MO_2)$[a] (Å)	$I(LiO_2)$[b] (Å)	z_{oxy}	R_p (%)	R_{wp} (%)	χ^2	$R(F^2)$
A	2.121(3)	2.629(4)	0.2589(2)	9.25	12.74	1.288	0.129
B	2.114(2)	2.633(3)	0.2591(1)	8.97	12.62	1.207	0.098

Site occupancy (%)	Li (3*b*)	Ni (3*b*) ≡ *y*	Li (3*a*)	Ni (3*a*)	Mn (3*a*)	Co (3*a*)	O (6*c*)
A	98.02(10)	1.98(10)	3.98(10)	30.72(10)	32.7(1)	32.7(1)	100
B	98.57(10)	1.43(10)	5.43(10)	28.55(10)	32.0(1)	32.0(1)	100

[a] $S(MO_2) = 2(1/3 - z_{oxy})c$ is the thickness of the metal–O_2 planes.
[b] $I(LiO_2) = c/3 - S(MO_2)$ is the thickness of the inter-slab space.

charge favors an increase of a, because Li($3a$) carries only a charge +e, so that the repulsive Coulomb potential with the neighboring transition-metal ions inside the slabs is smaller. The fact that a is smaller in sample B where the rate of substitution is smaller is thus evidence that the effective charge effect is dominant. In the same way, the presence of the Ni^{2+} ions in lithium plane leads to the stronger electrostatic attraction between oxygen and Li^+ or Ni^{2+}($3b$) ions in the LiO_2 inter-slab plane, hence the decrease of the LiO_2 inter-slab space, which can hinder lithium diffusion in $Li_{1+x}(Ni_{1/3}Mn_{1/3}Co_{1/3})_{1-x}O_2$. Two other structural parameters can be deduced from Rietveld analysis: $I(LiO_2)$ the thickness of the inter-slab space and $S(MO_2)$ the thickness of the metal–O_2 planes [34]

$$I(LiO_2) = \frac{c}{3} - S(MO_2), \tag{4}$$

$$S(MO_2) = 2\left(\frac{1}{3} - z_{oxy}\right)c. \tag{5}$$

As seen from Table 3, we find a, c, and $S(MO_2)$ are lower for sample B, which confirms that sample B has better structural integrity. Generally, the c/a value can also indicate the degree of trigonal distortion, a higher cation ordering being achieved when c/a value is higher than 4.899 [35]. For sample B, c/a is as high as 4.979, which clearly shows that the small excess in lithium in the synthesis process (nominal value $\eta = 1.10$) is an excellent approach to get better-ordered layered structure of the $Li_{1+x}(Ni_{1/3}Mn_{1/3}Co_{1/3})_{1-x}O_2$ powders and smaller concentration of Li^+/Ni^{2+} cation mixing. The results in Table 3 also suggest that $I(LiO_2)$ is higher in sample B. However, the error on this parameter is too high to give a definite conclusion on this particular parameter.

In the next section, we show that magnetic experiments reveal the same concentration of Ni^{2+} ions located on the $3b$-Li site, so that the structural model used for Rietveld refinements pictures well the atomic arrangement in the $Li_{1+x}(Ni_{1/3}Mn_{1/3}Co_{1/3})_{1-x}O_2$ lattices.

The surface morphology of $Li_{1+x}(Ni_{1/3}Mn_{1/3}Co_{1/3})_{1-x}O_2$ particle investigated by scanning electron microscopy is shown in Fig. 3a and b. The SEM micrographs display powders formed by aggregates of primary particles, which appear as small column-shaped particles. Typical dimensions of the small columned particle are 0.5 μm × 2 μm. It should be noted that the values of mean coherence length obtained from XRD analysis according to Eq. (1) is about one order of magnitude smaller than the dimensions of the primary particles, so that the primary particles should not be confused with crystallites. This small coherence length might be the reason for their good electrochemical performance as expected, because of the easier insertion/de-insertion and shorter pathway of diffusion for lithium-ion.

3.2. Magnetic properties

The temperature dependence of the reciprocal magnetic susceptibility $\chi_m^{-1} = H/M$ of both samples is presented in Fig. 4. The magnetization curves $M(H)$ are reported in Fig. 5a and b. Above 150 K, the curve $\chi_m^{-1}(T)$ shows a paramagnetic (PM) behaviour and the magnetization varies linearly with the applied magnetic field for both the $Li_{1+x}(Ni_{1/3}Mn_{1/3}Co_{1/3})_{1-x}O_2$ samples, so that χ_m is meaningful, i.e. $H/M = \partial H/\partial M$. The linear variations of χ_m^{-1} with T can be described by a Curie–Weiss law $\chi_m^{-1} = (T - \Theta_p)/C_p$, with Θ_p the Curie–Weiss temperature, and C_p the Curie constant related to the effective magnetic moment μ_{eff} by the relation $C_p = N \cdot \mu_{eff}^2/(3k_B)$ with k_B the Boltzmann constant and N the number of metal ions in one mole of product. The values of the two fitting parameters Θ_p and μ_{eff} for the two samples are reported in Table 4. Θ_p is negative in both compounds and this is an intrinsic property due to the fact that intrinsic magnetic interactions are mainly the intra-layer super-exchange interactions mediated via oxygen at 90° bonding

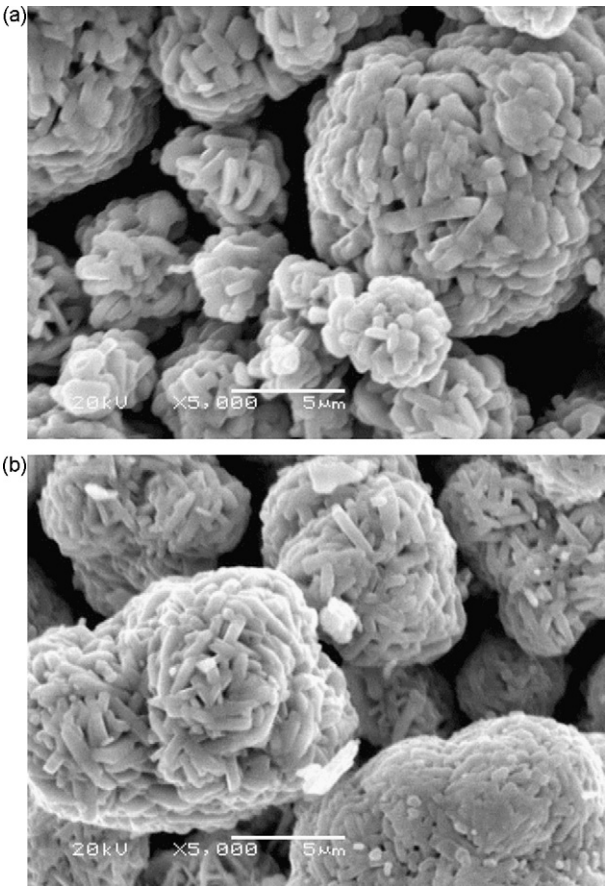

Fig. 3. SEM images of $Li_{1.02}(Ni_{1/3}Mn_{1/3}Co_{1/3})_{0.98}O_2$ sample A (a) and $Li_{1.04}(Ni_{1/3}Mn_{1/3}Co_{1/3})_{0.96}O_2$ sample B (b).

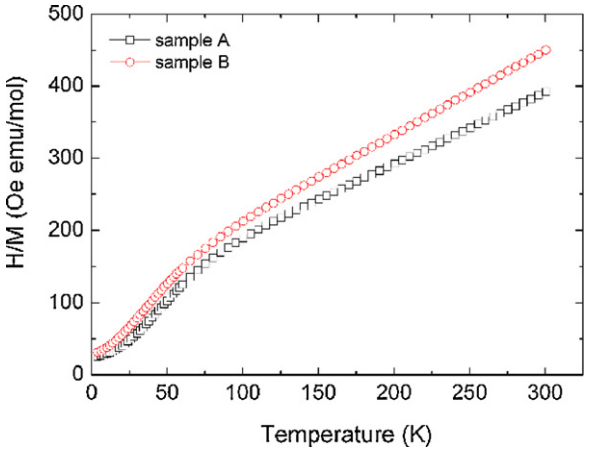

Fig. 4. Plot of the reciprocal magnetic susceptibility H/M for sample A and sample B. Data were collected with a magnetic field $H = 10$ kOe.

angle, and they are dominantly antiferromagnetic [19]. Taking into account that Ni^{3+} is in the low-spin state [36,37], the magnetic moments carried by Ni^{2+}, Ni^{3+}(low spin) and Mn^{4+} are 2.83, 1.73 and 3.87μ_B, respectively, while Co^{3+} is a diamagnetic ions in the $3d^6$-LS configuration in this material. Then, the theoretical value of the effective magnetic moment μ_{eff} of $Li_{1+x}(Ni_{1/3}Mn_{1/3}Co_{1/3})_{1-x}O_2$ ($x = 0.02$, 0.04) materials in the paramagnetic regime is:

$$\mu_{theor} = (0.287 * 2.83^2 + 0.04 * 1.73^2 + 0.327 * 3.87^2 + 0.327 * 0)^{1/2}\mu_B = 2.71\mu_B, \tag{6}$$

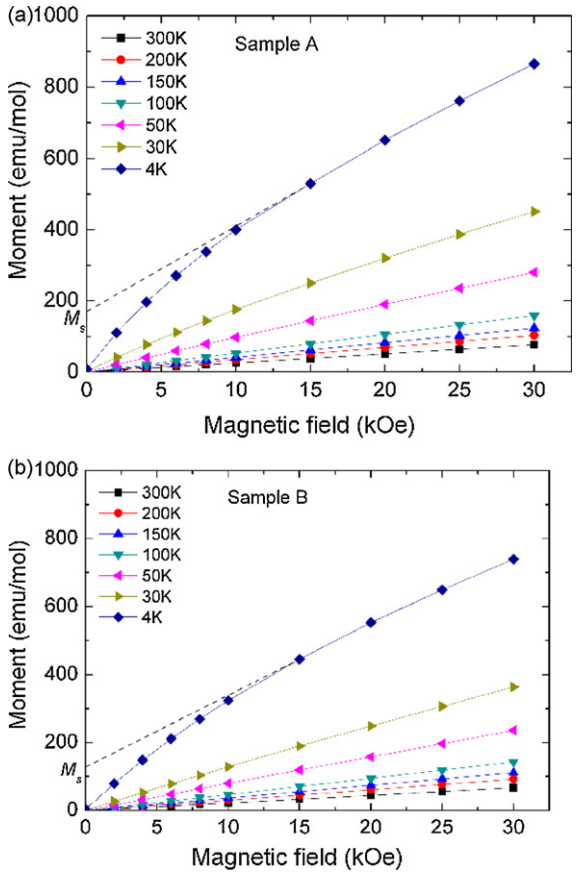

Fig. 5. Isothermal plots of the magnetization $M(H)$ for sample A (a) and sample B (b). M_s is the magnetic moment at saturation.

$$\mu_{\text{theor}} = (0.24 * 2.83^2 + 0.08 * 1.73^2 + 0.32 * 3.87^2 + 0.32 * 0)^{1/2} \mu_B = 2.64 \mu_B. \quad (7)$$

The experimental values of μ_{eff} for synthesized $Li_{1+x}(Ni_{1/3}Mn_{1/3}Co_{1/3})_{1-x}O_2$ are close to the theoretical value (see Table 4). Note this result provides an experimental proof that Li(3*a*) does not generate Ni^{4+} ions. In this material, Ni^{4+} can be obtained by delithiation. We know from the investigation of magnetic properties on these delithiated samples that Ni^{4+} is in the high spin state, and thus carries a big magnetic moment ($4.9\mu_B$). Therefore, if Ni^{4+} was formed instead of Ni^{3+}, μ_{theor} (calculated from Eqs. (6) and (7) with the second term replaced by $0.02*4.9^2$ and $0.04*4.9^2$, respectively) would be the same for both samples A and B, namely $2.775\mu_B$, which is in contradiction with the fact that the effective magnetic moment is lower in sample B than in sample A.

Although it is small, the difference between the theoretical value of μ_{eff} reported in Eqs. (6) and (7) and the experimental one is slightly larger for sample A than for sample B. To understand this effect, we note that the magnetization curves are no longer linear at temperature below 80 K. Note the first consequence is that the data in the temperature range $T < 80$ K in Fig. 4 do not have the meaning of the inverse of a magnetic susceptibility because $H/M \neq \partial H/\partial M$. Nevertheless, we have reported these data in Fig. 5a and b since they will be useful for discussion. For the moment, we just note that these deviations from linearity are related to the onset of an additional ferromagnetic contribution to the magnetization at low temperature, evidenced in the magnetization curves of samples A and B in Fig. 5a and b. Following our prior work [18], we attribute this feature to the $Ni^{2+}(3b)$ defects. The substitution of Ni for Li on 3*b* sites generates a 180° interlayer $Mn^{4+}(3a)$–O–$Ni^{2+}(3b)$ superexchange interaction that is ferromagnetic (FM) in nature, after the Goodenough rules [17]. This interaction is strong enough to generate a ferromagnetic spin freezing of the $Mn^{4+}(3a)$–$Ni^{2+}(3b)$ pair at low temperature, giving rise to an enhancement of the magnetization responsible for the decrease of $\chi^{-1}(T)$ at low temperature. We can then estimate that this ferromagnetic ordering of the $Mn^{4+}(3a)$–$Ni^{2+}(3b)$ pairs takes place approximately at the temperature $T_c \approx 40$ K where $\chi^{-1}(T)$ goes through an inflexion point. At lower temperature, the $Mn^{4+}(3a)$ spin and the $Ni^{2+}(3b)$ spin of a given pair will be spin-polarized ferromagnetically, so that the pair will respond to the magnetic field like an effective spin $S_{cl} = (S_{\text{Mn}} + S_{\text{Ni}}) = 5/2$, since the Mn^{4+} and Ni^{2+} ions carry a spin $S_{\text{Mn}} = 3/2$ and $S_{\text{Ni}} = 1$, respectively (and no orbital momentum, since it is quenched by the crystal-field). The relaxation time for the magnetic moment of such pairs is governed by [38]

$$\tau = \tau_0 \exp\left(\frac{KV}{k_B T}\right), \quad (8)$$

where $\tau_0 = \Gamma_0^{-1}$, Γ_0 is the attempt frequency of the order of 10^9 to 10^{13} s^{-1}, k_B is the Boltzmann constant; K and V are, respectively, the anisotropy constant and volume occupied by the ferromagnetic pair. The superparamagnetic blocking temperature (T_B) is usually defined as the temperature at which the measuring time of the equipment, t, is equal to the relaxation time τ, that is $t = \tau = \tau_0 \exp(KV/k_B T_B)$. Taking $t = 60$ s for the SQUID magnetometer and $\tau_0 = 10^{-10}$ s, we have [38]

$$25 k_B T_B = KV. \quad (9)$$

A typical order of magnitude for an anisotropy constant is provided by the value suited to cobalt that also crystallizes in the hexagonal structure: $K = 5 \times 10^5$ J m^{-3}, and the volume occupied by the ferromagnetic cluster is d^3 where d is the order of the length of the $Mn^{4+}(3a)$–$Ni^{2+}(3b)$ bond, say 0.5 nm. Then we expect that the blocking temperature is the order of $T_B = 0.4$ K, one order of magnitude smaller than the temperature 4.2 K that can be reached in our experiments. This is actually the main difference with the magnetic clusters either associated to impurity phases in ionic compounds or made on purpose for applications as magnetic recording media, in which case the particles are bigger, hence much higher blocking temperatures that are accessible to the experiments. This feature explains that the presence of ferromagnetic clusters in our particular case does not generate magnetic irreversibility. Indeed, there is no remanent magnetization in Fig. 5, and no difference has been detected either between field-cooled and zero-field cooled data (see the experimental procedures described in Section 2) reported in Fig. 4. On the other hand, under the application of the external magnetic field, the effective spin S_{cl} will give a magnetization that is approximately given by a Brillouin function $B_{S_{cl}}(x)$, the argument of which will be $x = g\mu_B S_{cl} H/(k_B T)$, with $g = 2$ the gyromagnetic factor of the spin. For $H = 30$ kOe at $T = 4.2$ K, $g\mu_B S_{cl}/(k_B T) = 2.3$, which is large enough so that $B_{S_{cl}}(x) \approx 1$ and the magnetization associated with the ferromagnetic clusters is approximately saturated. We can then estimate the amount of $Ni^{2+}(3b)$ defects as the ratio between the magnetic moment at saturation M_s of the ferromagnetic component of the magnetization, and the moment at saturation that

Table 4
Magnetic properties of two samples of $Li_{1+x}(Ni_{1/3}Mn_{1/3}Co_{1/3})_{1-x}O_2$ ($x = 0.02, 0.04$).

Samples	C_p (emu K mol^{-1})	Θ_p (K)	μ_{theor} (μ_B)	μ_{eff} (μ_B)	M_s (emu mol^{-1})	$Ni^{2+}(3b)$
A	0.99	−89	2.71	2.83	170	1.88%
B	0.85	−80	2.64	2.62	128	1.50%

the sample would have if all the Mn and Ni ions were saturated ferromagnetically, namely

$$g\mu_B(0.327 * S_{Mn^{4+}} + 0.287 * S_{Ni^{2+}} + 0.04 * S_{Ni^{3+}}) = 1.60\mu_B, \quad (10)$$

$$g\mu_B(0.32 * S_{Mn^{4+}} + 0.24 * S_{Ni^{2+}} + 0.08 * S_{Ni^{3+}}) = 1.52\mu_B \quad (11)$$

per chemical formula unit. M_s has been estimated from the linear extrapolation to $H \to 0$ of the isothermal magnetization curve $M(H)$ at $T = 4.2$ K taken in the range $20 < H < 30$ kOe, which satisfies the condition of saturation for the ferromagnetic component. The results for the estimation of the rate of substitution y deduced from this magnetic analysis are reported in Table 4. They agree with the results deduced from Rietveld refinements for the two samples investigated. For instance, in the case of the sample A, we find $M_s = 170$ emu mol^{-1} (Fig. 5a), which amounts to a magnetic moment per formula $0.03\mu_B$. So the concentration of Ni^{2+} at 3*b* sites can be calculated as 0.03/1.60 = 1.88%. For sample B, we find $M_s = 128$ emu mol^{-1} and we calculate its concentration of Ni^{2+} at 3*b* sites as 1.50%, which is in agreement with the result obtained from Rietveld refinement (1.43%). In the paramagnetic regime, the ferromagnetic $Mn^{4+}(3a)$–O–$Ni^{2+}(3b)$ pairing enhances the effective magnetic moment of the material. That is why the difference between experimental and theoretical values of μ_{eff} increases with the concentration y of such ferromagnetic bonds, and is larger for sample A. On one hand, the larger value $x = 0.04$ in sample B implies that a fraction of Li^+ ions have substituted to magnetic nickel and manganese ions, so that μ_{eff} is smaller: see Eqs. (6) and (7) and the experimental values in Table 4. On another hand, a larger excess of lithium in the product counteracts this cation mixing (smaller value of y), and thus reduces the concentration of ferromagnetic $Mn^{4+}(3a)$–$Ni^{2+}(3b)$ interactions. This is actually a general trend in these materials, since it has been observed also in $Li_{1+x}(Ni_{0.5}Mn_{0.5})_{1-x}O_2$ [21].

3.3. Electrochemical characteristics

Electrochemical properties of $Li_{1+x}(Ni_{1/3}Mn_{1/3}Co_{1/3})_{1-x}O_2$ samples have been investigated in standard CR2032 coin cells using 1.0 mol L^{-1} $LiPF_6$/(EC:DEC = 1:1, v/v) as the electrolyte. The cells were galvanostatically cycled at room temperature between 3.0 and 4.3 V vs. Li^0/Li^+ at constant current of C/2-rate (ca. 75 mA g^{-1}) for charging and 1 C-rate (ca. 150 mA g^{-1}) for discharging. Fig. 6a and b display the typical charge–discharge profiles of the $Li_{1+x}(Ni_{1/3}Mn_{1/3}Co_{1/3})_{1-x}O_2$ samples for the 8th and 18th cycles. As expected, these results show that charge and discharge curves for cells A and B are representative of the $Li_{1+x}(Ni_{1/3}Mn_{1/3}Co_{1/3})_{1-x}O_2$ electrode material with quite a smooth shape of the potential vs. capacity plots.

Both samples exhibit the initial charge and discharge capacity of 162 mAh g^{-1} and 150 mAh g^{-1}, respectively, which provides coulombic efficiency of 93% and irreversible capacity loss 12 mAh g^{-1} during the initial cycle. The discharge capacity at the 1 C-rate has a value in the vicinity of 147 mAh g^{-1} for the 8th cycle. The coulombic efficiency is 99% and the irreversible capacity loss is 1 mAh g^{-1} for the 18th cycle. More than 95% of its initial capacity has been retained after 30 cycles at 1 C-rate.

The electrochemical storage energy and intercalation mechanism in LNMCO is attributable to the Ni^{2+}/Ni^{4+} redox reaction pair. This was confirmed in our previous reports on the $LiNi_yMn_yCo_{1-2y}O_2$ electrode materials [18]. The oxidation states of Ni, Mn and Co were confirmed to be 2+, 4+ and 3+ in the pristine material (discharge state). Mn^{4+} is unchanged during charge, while the oxidation state of Ni changes from 2+ to 4+ followed by the oxidation of Co^{3+} to Co^{4+} at the end of charge. In the $LiNi_yMn_yCo_{1-2y}O_2$ lattice, the substituted Mn for Co ions only ensures the structural integrity of the materials with better stabilization of the layered

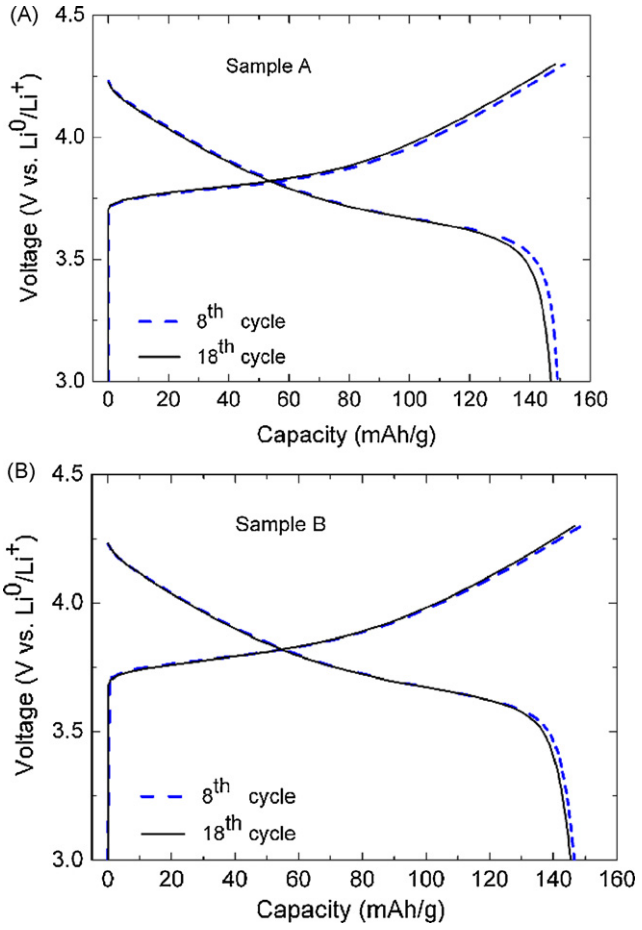

Fig. 6. Charge and discharge curve of Li/1.0 mol L^{-1} $LiPF_6$ in EC-DEC/$Li_{1+x}(Ni_{1/3}Mn_{1/3}Co_{1/3})_{1-x}O_2$ coin cells at room temperature. Experiments were carried out at constant current C/2-rate charge and 1 C-rate discharge in the voltage range of 3.0–4.3 V. Blue dashed lines represent the 8th cycle, while black full lines are the 18th cycle for sample A (graph a) and sample B (graph b).

structure and less cation mixing between Li^+ and Ni^{2+}. This is the reason for better capacity retention and cyclability of the LNMCO electrode materials.

We find that both samples prepared in this work exhibit similar electrochemical performance despite the significant difference in synthetic conditions. This is primarily due to the good structural arrangement of these electrode materials. In fact, with a concentration of $Ni^{2+}(3b)$ defects lower than 2 mol%, we do not observe any influence of such cation mixing on the electrochemical properties of $Li_{1+x}(Ni_{1/3}Mn_{1/3}Co_{1/3})_{1-x}O_2$ ($x = 0.02, 0.04$) materials. This is the net effect of the minimum disorder in the interlayer space. Another proof that the $Ni^{2+}(3b)$ defects do not impact the electrochemical performance at such low substitution rate is provided by the comparison with the results obtained for the same material with $[Ni^{2+}(3b)] = 1.24\%$ [39], to our knowledge the only case reported with $[Ni^{2+}(3b)]$ smaller than in our samples. In this earlier work, the cut-off voltage was 4.3 V, the same as in the present work. The initial discharge capacity was found to be 159 mAh g^{-1} that could be compared to our case, despite the fact that it was measured at current density 20 mAh g^{-1}, which corresponds to a slower rate (C/8 against 1 C in the present work). Let us recall, however, that increasing $[Ni^{2+}(3b)]$ above 2% deteriorates the electrochemical performance. This has been proved in Ref. [40], since a degradation of the performance was found upon increasing $[Ni^{2+}(3b)]$ in the whole range $2.2\% \leq [Ni^{2+}(3b)] \leq 4.9\%$. A second reason for the excellent electrochemical performance is the morphology of the

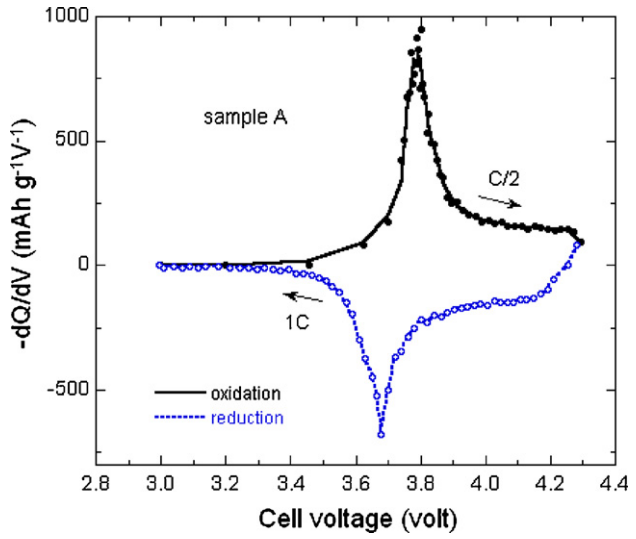

Fig. 7. Differential capacity $(-\partial Q/\partial V)$ vs. cell potential of the Li//$Li_{1.02}(Ni_{1/3}Mn_{1/3}Co_{1/3})_{0.98}O_2$ (A-sample) coin cell presented in Fig. 6a. Upon charging at C/2-rate the cell displays a major oxidation peak at 3.79 V, while the reduction peak occurs at 3.68 V upon discharging at 1 C-rate.

$Li_{1+x}(Ni_{1/3}Mn_{1/3}Co_{1/3})_{1-x}O_2$ active particles that appear under the form of the elongated shape crystallites.

Fig. 7 shows the differential capacity $(-\partial Q/\partial E)$ vs. cell potential E of the Li//$Li_{1+x}(Ni_{1/3}Mn_{1/3}Co_{1/3})_{1-x}O_2$ ($x = 0.02$, A-sample) coin cell calculated from data presented in Fig. 6a. Upon charging at C/2-rate the cell displays a major oxidation peak at 3.79 V, while the reduction peak occurs at 3.68 V upon discharging at 1 C-rate. Similar electrochemical data have been obtained for sample B and analysed as follows. As reported many times in the literature, the oxidation peak at ca. 3.8 V with the corresponding reduction peak at 3.7 V are typical of the Ni^{2+}/Ni^{4+} redox reaction in the Li–Ni–Mn–Co oxide lattice [11,18]. However, the asymmetry toward the high potential side is due to the partial redox contribution from Co^{3+} to Co^{4+} that corresponds to the second electron transfer.

The cell voltage of an electrochemical cell is defined by the Gibbs free energy variation associated with one mole of reaction $\Delta G = -zFE$, where F is the Faraday constant, z the number of electrons in the redox reaction equation, and E is the cell voltage. The lattice gas model is most commonly used to describe the intercalation reaction. In this picture the host plays two roles: it provides a set of lattice sites where guest atoms reside and it determines the interaction between guest atoms. The composition dependence of the cell voltage derives from the master equation giving the free energy variation, and is given by [41]

$$E = E_0 + \frac{RT}{F}\ln\frac{x'}{x_{\max} - x'} + \frac{RT}{F}\gamma x', \tag{12}$$

where R is the universal gas constant. The lithium ions that can be removed or inserted are the Li^+ ions in the (3*b*) sites. The electrochemical force is not strong enough to move Ni^{2+} in the (3*b*) sites, and Li^+ from a (3*a*) site. Therefore only the lithium in the (3*b*) sites should be taken into account, and x' is their concentration at the current stage of the lithiation/delithiation process. x_{max} is the highest Li concentration in the (3*b*) sites of the solid solution, supposed to be ideal so that the activity coefficients are set to unity. γ is a lateral interaction parameter that is introduced to represent the effects of the interactions in a two-dimensional process. Eq. (12) with its second term is the Nernst equation associated to the Frumkin's isotherm that describes adsorption phenomena taking into account interactions between the adsorbed species [42,43].

Finite positive γ values corresponds to repulsive interaction; $\gamma = 0$ signifies the absence of any interaction; negative value of $\gamma > -4$ relate to attractive interaction between the intercalation sites. At $\gamma_c = -4$, a critical state arises and for $\gamma \le -4$, the interactions are so intensive that they lead to the existence of two-phase reactions. E_0 is the standard potential. Usually, it is defined as the value of E at $x = 0.5$ for intercalation compounds, but Eq. (12) shows that this is true only if $x_{max} = 1$ and $\gamma = 0$. As we shall see hereunder, due to the fact that we have more than one redox process in the present case, we cannot set $x_{max} = 1$ for all of them, and $\gamma = 0$. Therefore, we are led to define E_0 as the potential at which $E(x)$ (or equivalently E as a function of the capacity, to make closer contact with experiments in Fig. 6) goes through an inflexion point, namely at $x_{max}/2$. Intercalation is sometimes more complex, since sorption must operate against the cohesive forces between the Van der Waals gap [44]. In such a case, another correction term $-p/x$ has to be added in the second member of Eq. (12), which amounts to an intercalation pressure p [45]. In this work, however, we are dealing with a lamellar oxide, for which p is negligible. This is evidenced by the very small change of the lattice parameters during charge and discharge [46,47]. To simplify the notations, it is convenient to consider one mole of product, so that $\partial Q/\partial x' = -F$, in which case the differential capacity $-\partial Q/\partial E = (-\partial Q/\partial x')(\partial x'/\partial E)$ can be written:

$$C = F\frac{\partial x'}{\partial E}. \tag{13}$$

By solving the derivative form in Eq. (12), one obtains

$$C = \frac{F^2}{RT}\sum_i \left[\gamma_i + \frac{x_{\max,i}}{x'(x_{\max,i} - x')}\right]^{-1}. \tag{14}$$

We consider two redox processes: first: Ni^{2+}/Ni^{4+} via Ni^{3+} and second: Co^{3+}/Co^{4+}, labelled by the index $i = 1, 2$, respectively, in Eq. (14). At equilibrium, due to the difference in the redox potentials, only the first redox reaction takes place in the first step of delithiation, starting from the concentration:

$$x_{\max,1} = 1 - y \tag{15}$$

of lithium on (3*b*) sites, and we can consider that this process continues upon delithiation, until all the nickel ions have been converted into Ni^{4+}. The initial concentration of Ni^{2+} that can be converted into Ni^{3+} is the total amount to nickel $(1-x)/3$ minus the Ni that is already in the trivalent state, and we have determined in Section 3.1 that it is $\xi[Ni^{3+}] = 2x$. Then all the Ni^{3+} ions in concentration $(1-x)/3$, can be converted to Ni^{4+}. The concentration of lithium on (3*b*) sites at the end of this process is then:

$$x_{\max,2} = (1-y) - \left[\frac{1-x}{3} - 2x\right] - \frac{1-x}{3} = \frac{1}{3} - y + \frac{8x}{3}. \tag{16}$$

Note that we have decomposed the redox process in two distinct sequential steps $Ni^{2+} \rightarrow Ni^{3+}$ and then $Ni^{3+} \rightarrow Ni^{4+}$ just for simplicity to calculate $x_{max,2}$, but it does not have to be the real process. In practice, part of the nickel may be already ionized in the Ni^{4+} before all nickel ions will be in the Ni^{3+} state. The value of $x_{max,2}$, however, is unaffected, and is still given by Eq. (16). On another hand, at this stage, all the Co ions are still in the Co^{3+} state of charge. Only an additional decrease of x' converts Co^{3+} into Co^{4+}. Then the differential capacity can be deduced from Eq. (14), taking Eqs. (15) and (16) into account, with γ_1, γ_2 the fitting parameters. Fig. 8 shows both the experimental and best fit of the differential capacity corresponding to the discharge curve of the Li//B-$Li_{1+x}(Ni_{1/3}Mn_{1/3}Co_{1/3})_{1-x}O_2$ ($x = 0.04$) coin cell presented in Fig. 6b. The fit has been achieved for the interaction factor associated to each redox process $\gamma_1 = -3.71$, $\gamma_2 = -3.00$. After Fig. 6b, the standard potentials being deduced from $E(x_{max,i}/2)$ according to Eq. (12) are $E_{0,1} = 3.722$ V and $E_{0,2} = 3.932$ V. Note that the value of γ_1 associated to the Ni^{2+}/Ni^{4+} redox reaction is not far from the critical value ($\gamma_c = -4$). Such attractive interactions have been derived

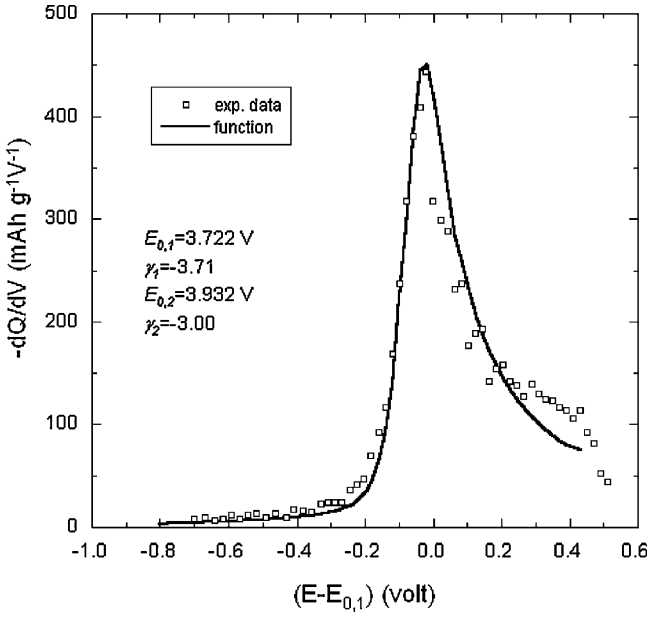

Fig. 8. Differential capacity vs. cell potential for the discharge process of the Li//$Li_{1.04}(Ni_{1/3}Mn_{1/3}Co_{1/3})_{0.96}O_2$ (B-sample) coin cell presented in Fig. 6b. The best fit of the differential capacity is obtained using Eqs. (12) and (14) with two redox processes with standard potential $E_{0,1}$ = 3.722 V, $E_{0,2}$ = 3.932 V and interaction factor $\gamma_1 = -3.71$, $\gamma_2 = -3.00$.

in other Li intercalation systems, actually each time the intercalation of lithium is characterized by strong interactions between the intercalated ions and the sites of the intercalated ions. Sometimes this attractive interaction is so strong that it drives a first order transition corresponding to the separation in two phases, which corresponds to the critical case $\gamma = -4$: This is the situation met for instance in the delithiation process of $LiFePO_4$ [48]. In the present case the interaction is smaller, so that the system remains single-phased, but it is still important. After Eq. (12), the differential capacity would diverge at $E_{0,1}$ for this critical value of γ_1. Since γ_1 is smaller, the divergence has been softened to a maximum, but still the proximity to the singularity is responsible for the fact that the maximum at $E = E_{0,1}$ is sharp and dominates the curve in Fig. 8. That is why we have chosen $E - E_{0,1}$ as the abscissa in this figure. On another hand, the value of γ_2 is already far enough from γ_c, so that the contribution of the differential capacity is so much broadened that it does not lead to a secondary maximum in the curve in Fig. 8. The fit is very good, except at high potential $E > E_{0,2}$. This small disagreement can be attributed to the fact that all the equations suppose thermal equilibrium, while the 1 C-rate used in the experiments is too fast to allow for the equilibrium to be reached for the Co^{3+}/Co^{4+} redox process. The dissymmetry in the curves recorded during the charge and the discharge in Fig. 7 is indeed the proof that this equilibrium has not been reached. These results reveal that the insertion/de-insertion of lithium ions in the layered $Li_{1+x}(Ni_{1/3}Mn_{1/3}Co_{1/3})_{1-x}O_2$ framework occurs with relatively strong interactions between the moving Li-ions and the sites of the host matrix. However, the second step appears to be less interactive due to the large concentration of Li vacancies in the interlayer space at elevated potential.

Fig. 9 displays the plots of the capacity retention against cycle number for $Li_{1+x}(Ni_{1/3}Mn_{1/3}Co_{1/3})_{1-x}O_2$ (x = 0.02, 0.04) electrode materials. Cycling was carried out galvanostatically at constant charge current density C/2 and at 1 C discharge rate between 3.0 and 4.3 V. The capacity retention for both electrodes appears to be similar. The practical discharge capacity slightly decreases upon cycling life of the lithium cells. Considering a linear decrease of the

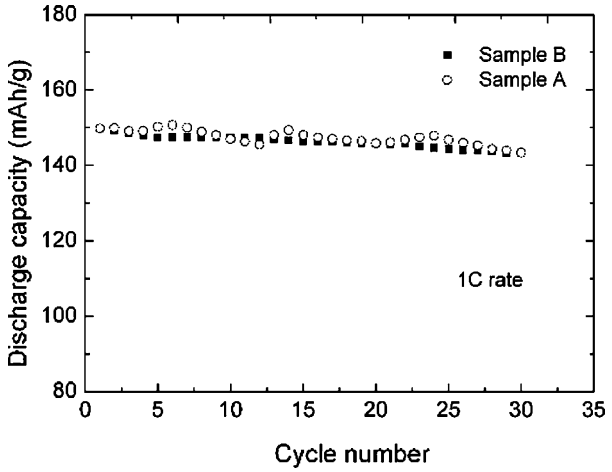

Fig. 9. Cycling performance of the lithium coin cells containing $Li_{1+x}(Ni_{1/3}Mn_{1/3}Co_{1/3})_{1-x}O_2$ (x = 0.02, 0.04). Experiments were carried out at 1 C discharge rate in the potential between 4.3 and 3.0 V. Plots of the capacity retention vs. cycle number are almost identical for samples A and B.

capacity of the form

$$C = C_0 - An, \tag{17}$$

where C_0 is the initial capacity, A is the rate of capacity loss, and n the number of cycles, the best fit of the curves in Fig. 9 gives a rate of 0.15% per cycle for the $Li_{1+x}(Ni_{1/3}Mn_{1/3}Co_{1/3})_{1-x}O_2$ (x = 0.02, 0.04) electrodes synthesized by co-precipitation method.

4. Conclusion

The layered $Li_{1+x}(Ni_{1/3}Mn_{1/3}Co_{1/3})_{1-x}O_2$ compound was synthesized via co-precipitation method with different Li/M molar ratios. XRD, SQUID and charge–discharge characterizations show that the structural, magnetic and electrochemical profiles are sensitive to the synthetic conditions. The optimized performance of the $Li_{1+x}(Ni_{1/3}Mn_{1/3}Co_{1/3})_{1-x}O_2$ electrode was obtained from the lithium-rich sample B. Concentrations of Ni^{2+} located onto 3b sites, which account for the cation mixing, estimated from the magnetization curves are 1.88% and 1.50% for samples A and B, respectively. These values agree well with the Rietveld refinement results, e.g. 1.98% and 1.43%, respectively. Due to the weak cation mixing in samples, the electrochemical performance is identical for $Li_{1+x}(Ni_{1/3}Mn_{1/3}Co_{1/3})_{1-x}O_2$ samples prepared by co-precipitation method with synthetic conditions $1.10 \geq \eta \geq 1.05$. An initial discharge capacity of 150 mAh g^{-1} was delivered at 1 C-rate in the cut-off voltage of 3.0–4.3 V and more than 95% of its initial capacity was retained after 30 cycles. Finally, we state that a cation mixing below 2% can be considered as the threshold for which the electrochemical performance does not change for $Li_{1+x}(Ni_{1/3}Mn_{1/3}Co_{1/3})_{1-x}O_2$ (x = 0.02, 0.04).

References

[1] J.B. Goodenough, Advances in Lithium-ion Batteries, Kluwer Academic Publ., New York, 2002.
[2] K. Amine, C.H. Chen, J. Liu, M. Hammond, A. Jansen, D. Dees, I. Bloom, D. Vissers, G. Henriksen, J. Power Sources 97–98 (2001) 684.
[3] T. Ohzuku, Y. Makimura, Chem. Lett. 30 (2001) 642.
[4] N. Yabuuchi, T. Ohzuku, J. Power Sources 119–121 (2003) 171.
[5] Z. Lu, D.D. MacNeil, J.R. Dahn, Electrochem. Solid State Lett. 4 (2001) A200.
[6] D.D. MacNeil, Z. Lu, J.R. Dahn, J. Electrochem. Soc. 149 (2002) A1332.
[7] J.-H. Kim, C.S. Yoon, Y.-K. Sun, J. Electrochem. Soc. 150 (2003) A538.
[8] B.J. Hwang, Y.W. Tsai, D. Carlier, G. Ceder, Chem. Mater. 15 (2003) 3676.
[9] I. Kobayashi, H. Sakaebe, H. Kageyama, K. Tatsumi, Y. Arachi, T. Kamiyama, J. Mater. Chem. 13 (2003) 90.
[10] W.-S. Yoon, C.P. Grey, M. Balasubramanian, X.-Q. Yang, D.A. Fischer, J. McBreen, Electrochem. Solid-State Lett. 7 (2004) A53.

[11] I. Belharouak, Y.-K. Sun, J. Liu, K. Amine, J. Power Sources 123 (2003) 247.
[12] K.M. Shaju, P.G. Bruce, J. Power Sources 174 (2007) 1201.
[13] P.S. Whitfield, I.J. Davidson, L.M.D. Cranswick, I.P. Swainson, P.W. Stephens, Solid State Ionics 176 (2005) 463.
[14] K.-S. Lee, S.-T. Myung, J. Prakash, H. Yashiro, Y.-K. Sun, Electrochim. Acta 53 (2008) 3065.
[15] C.M. Julien, A. Ait-Salah, A. Mauger, F. Gendron, Ionics 12 (2006) 21.
[16] N. Amdouni, F. Gendron, A. Mauger, H. Zarrouk, C.M. Julien, Mater. Sci. Eng. B 129 (2006) 64.
[17] J.B. Goodenough, Magnetism and the Chemical Bond, Wiley, New York, 1963.
[18] A. Abdel-Ghany, K. Zaghib, F. Gendron, A. Mauger, C.M. Julien, Electrochim. Acta 52 (2007) 4092.
[19] A. Abdel-Ghany, A. Mauger, F. Gendron, K. Zaghib, C.M. Julien, ECS Trans. 3 (2007) 137.
[20] A.R. Nichols, J.H. Walton, J. Am. Chem. Soc. 64 (1942) 1866.
[21] S.-T. Myung, S. Komaba, K. Kurihara, K. Hosoya, N. Kumagai, Y.-K. Sun, I. Nakai, M. Yonemura, T. Kamiyama, Chem. Mater. 18 (2006) 1658.
[22] L. Zhang, X. Wang, T. Muta, D. Li, H. Noguchi, M. Yoshio, R. Ma, K. Takada, T. Sasaki, J. Power Sources 162 (2006) 629.
[23] J. Choi, A. Manthiram, J. Electrochem. Soc. 152 (2005) A1714.
[24] Y.M. Todorov, K. Numata, Electrochim. Acta 50 (2004) 495.
[25] B.H. Toby, J. Appl. Cryst. 34 (2001) 210.
[26] P. Samarasinghab, D.-H. Tran-Nguyen, M. Behma, A. Wijayasinghe, Electrochim. Acta 53 (2008) 7995.
[27] A. Wijayasinghe, B. Bergman, C. Lagergren, Solid State Ionics 177 (2006) 175.
[28] A. Rougier, P. Gravereau, C. Delmas, J. Electrochem. Soc. 143 (1996) 1168.
[29] K.S. Park, M.H. Cho, S.J. Jin, K.S. Nahm, Electrochem. Solid-State Lett. 7 (2004) A239.
[30] J.R. Dahn, U. von Sacken, C.A. Michal, Solid State Ionics 44 (1990) 87.
[31] J.N. Reimers, E. Rossen, C.D. Jones, J.R. Dahn, Solid State Ionics 61 (1993) 335.
[32] T. Ohzuku, A. Ueda, M. Nagayama, J. Electrochem. Soc. 140 (1993) 1862.
[33] R.D. Shannon, Crystallogr. Acta A32 (1976) 751.
[34] N. Tran, L. Croguennec, C. Jordy, P. Biensan, C. Delmas, Solid State Ionics 176 (2005) 1539.
[35] K.M. Shaju, G.V. Subba Rao, B.V.R. Chowdari, Electrochim. Acta 48 (2002) 145.
[36] N.A. Chernova, M. Ma, J. Xiao, M.S. Whittingham, J. Breger, C.P. Grey, Chem. Mater. 19 (2007) 4682.
[37] M. Ma, N.A. Chernova, B.H. Toby, P.Y. Zavalij, M.S. Whittingham, J. Power Sources 165 (2007) 517.
[38] X.X. Zhang, J.M. Hernandez, J. Tejada, R.F. Ziolo, Phys. Rev. B 54 (1996) 4101.
[39] M.-H. Lee, Y.-J. Kang, S.-T. Myung, Y.-K. Sun, Electrochim. Acta 50 (2004) 939.
[40] Y.-J. Shin, W.-J. Choi, Y.-S. Hong, S. Yoon, K.S. Ryu, S.H. Chang, Solid State Ionics 177 (2006) 515.
[41] P.P. Prosini, M. Lisi, D. Zane, M. Pasquali, Solid State Ionics 148 (2002) 45.
[42] J.O.M. Bockris, A.K.N. Reddy, M. Gamboa-Aldeco, Modern Electrochemistry, Second edition, Fundamentals of Electronics, vol. 2A, Kluwer Acad., 2000, p. 1070.
[43] R. Parsons, Russ. J. Electrochem. 37 (2001) 549 (from Elektrokhimiya 37 (2001) 647).
[44] J.R. Dahn, U. von Sacken, M.W. Juzkow, H. Al-Janaby, J. Electrochem. Soc. 138 (1991) 2207.
[45] M.B. Armand, Materials for Advanced Batteries, Plenum Press, New York, 1980.
[46] N. Yabuuchi, Y. Makimura, T. Ohzuku, J. Electrochem. Soc. 154 (2005) A314.
[47] J.-M. Kim, H.-T. Chung, Electrochim. Acta 49 (2004) 937.
[48] C.V. Ramana, A. Mauger, F. Gendron, C.M. Julien, K. Zaghib, J. Power Sources 187 (2009) 555.